AD_____

Award Number: W81XWH-12-1-0475

TITLE: An Injectable Method for Posterior Lateral Spine Fusion

PRINCIPAL INVESTIGATOR: Dr. Elizabeth Olmsted-Davis

CONTRACTING ORGANIZATION: Baylor College of Medicine
Houston, TX 77030

REPORT DATE: September 2013

TYPE OF REPORT: Annual Report

PREPARED FOR: U.S. Army Medical Research and Materiel Command
Fort Detrick, Maryland 21702-5012

REPORT DOCUMENTATION PAGE

Form Approved
OMB No. 0704-0188

1. REPORT DATE	2. REPORT TYPE	3. DATES COVERED
September 2013	Annual Report	01 September 2012-31 August 2013

4. TITLE AND SUBTITLE

An Injectable Method for Posterior Lateral Spine Fusion

5a. CONTRACT NUMBER

5b. GRANT NUMBER
W81XWH-12-1-0475

5c. PROGRAM ELEMENT NUMBER

6. AUTHOR(S)
Dr. Elizabeth A. Olmsted-Davis, Dr. Jennifer West, Dr. Alan R. Davis, Dr. Eva Sevick-Muraca.

E-Mail: edavis@bcm.edu

5d. PROJECT NUMBER

5e. TASK NUMBER

5f. WORK UNIT NUMBER

7. PERFORMING ORGANIZATION NAME(S) AND ADDRESS(ES)
Baylor College of Medicine, Houston, TX 77030

8. PERFORMING ORGANIZATION REPORT NUMBER

9. SPONSORING / MONITORING AGENCY NAME(S) AND ADDRESS(ES)
U.S. Army Medical Research and Materiel Command
Fort Detrick, Maryland 21702-5012

10. SPONSOR/MONITOR'S ACRONYM(S)

11. SPONSOR/MONITOR'S REPORT NUMBER(S)

12. DISTRIBUTION / AVAILABILITY STATEMENT
Approved for Public Release; Distribution Unlimited

13. SUPPLEMENTARY NOTES

14. ABSTRACT
The central hypothesis of this application is that posterolateral spine fusion can be successfully achieved with a novel and simple minimally invasive percutaneous injection. We propose that this can be done by injection of AdBMP2 transduced human fibroblasts possessing an icasp9$_M$ that have been micro-encapsulated with osteoclast degradable hydrogel into the desired fusion site. During this first year, we have initiated the identification of the phenotype of the monocyte-like cells that appear to be capable of bone degradation. We have demonstrated in MSCs, which have a stably integrated icasp9$_M$, can be rapidly induced to undergo apoptosis, after delivery of a chemical inducer of dimerization (CID) after encapsulation in PEG hydrogel. The next step is to start *in vivo* testing of this system. Additionally we have developed the methodology to non-invasively locate the hydrogel microsphere placement, optically, with respect to the newly forming bone. This has lead to a publication. We have also initiated studies to fuse the spine using our cell based gene therapy system encapsulated in the PEG hydrogel microspheres, in both mouse and rat. We will continue to complete these studies in the upcoming year.

15. SUBJECT TERMS
BMP2, Spine fusion, PEG Hydrogel, Gene Therapy, Adenovirus.

16. SECURITY CLASSIFICATION OF:			17. LIMITATION OF ABSTRACT	18. NUMBER OF PAGES	19a. NAME OF RESPONSIBLE PERSON
a. REPORT	b. ABSTRACT	c. THIS PAGE			USAMRMC
U	U	U	UU	18	19b. TELEPHONE NUMBER *(include area code)*

Table of Contents

INTRODUCTION: The treatment of many spinal problems involves stabilization of the spine by applying bone grafts to the posterior elements of the spine. The objective of these procedures is to induce bone to bridge between adjacent vertebral bodies and "fuse" the vertebrae into a larger bone mass. Posterolateral fusion of the spine is the most commonly performed of all the types of spine fusion and is useful for the treatment of scoliosis, instability and painful degenerative conditions of the spine. We recently demonstrated that adenovirus transduced cells expressing BMP2, when injected into the paraspinous musculature, could rapidly form new bone at the targeted location and efficiently fuse vertebral bone at a desired site, within 2 weeks. Encapsulation of these cells in poly(ethylene glycol)-diacrylate (PEGDA) hydrogels allowed for longer survival of the cells *in vivo*, did not result in inflammation, which otherwise completely ablate new bone formation/fusion, and maintained the cells at the target location. Thus our preliminary data demonstrates the ability to induce new bone formation at the desired fusion location without need for any surgical intervention. Here we propose to engineer additional safety features into the material by using an inducible caspase 9 ($icasp9_M$), which when activated will induce apoptosis within the transduced cells. Further, the hydrogel will also possess an osteoclast selective protease site which allows for removal of the biomaterial during bone remodeling.

BODY:

Task 1: To characterize the ability of the molecular therapy system to rapidly induce fusion of the new bone with the vertebra, through induction of osteoclast progenitors (OCP) – monocyte progenitors. The proposed studies in this aim are an extension from our previous findings that monocyte-like cells that are not multinucleated osteoclasts were observed at the fusion site between the new heterotopic bone, and skeletal bone (figure 1). These cells appeared to be contributing to the remodeling of the fusion structure, and may be critical to enhancing fusion between the two bones. We propose that if we could characterize and isolate

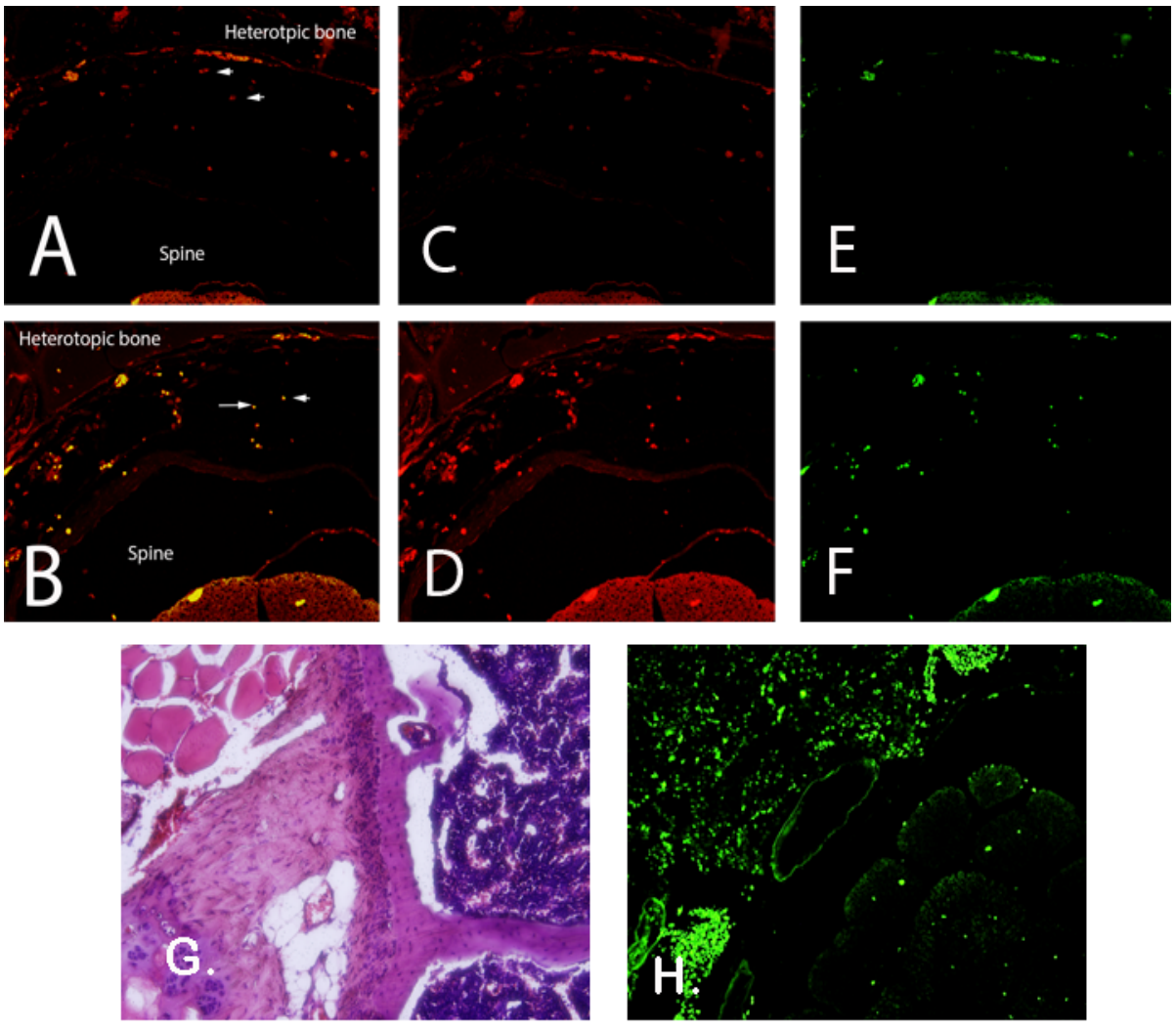

Figure 1: Representative photomicrographs of tentative vertebral fusion with the heterotopic bone. The slides were immunostained for **(A and C)** CD11b (red), **(A and E)** fractalkine (green) and merged in **(A)**. In panels **(B and D)** fractalkine (red), **(B and E)** LyC6 (green), and **(G)** hematoxylin and eosin for viewing. Panel H depicts a nerve with positive staining for LyC6 in the perineurium. These are representative photomicrograph (10X) of a sample taken 4 weeks after the initial injection of AdBMP2 transduced cells.

these cells, they may be beneficial in enhancing spine fusion, in other model systems as well as our own. One of the first steps is to determine their phenotype and determine if they are actually specialized M2 macrophages expanded to aid in matrix remodeling and fusion.

Therefore we have secured animal approval for the studies, and performed spine fusion in mice to generate tissue sections for initial phenotypic characterization of these spines. In these experiments, mice (n= 4) were injected with AdBMP2 or Adempty transduced cells and then spines isolated at weekly intervals (1-6 weeks) and serial sections generated, that represent the fusion process in the animals. We then initiated immunohistochemical staining with key antibodies that will be used for fluorescence activated cell sorting (FACs). These antibodies (CD11b ^{lo}, fractalkine^{+}, Ly6C^{+}), are surface antigens that can readily allow us to sort populations of cells for testing in bone resorption assays. After initial optimization of the antibodies, we observed co-localization of fractalkine^{+} and Ly6C^{+} in the cells, but as expected they were not expressing CD11b (figure 1). These cells were found lining the junction between the heterotopic bone and the new bone (figure 1, panel B). What was further intriguing was that cells associated with the perineurium of the nerve were also LyC6^{+} but not fractalkine^{+}. It is unclear whether these cells may function as an earlier progenitor, or whether they are just a separate population. We will continue to characterize this phenptype.

The next step is to isolate and further characterize the phenotype of these cells specifically to demonstrate their potential M2 nature. Also we will collect the various positive and negative populations and confirm their bone resorption ability using a standard assay kit (Bone Resorption Assay Kit; CosmoBio Co, Ltd) that uses a fluoresceinated calcium phosphate-coated plate. Additionally, we will isolate and test these cells *in vitro* to determine whether they respond to Lipopolysaccharide (LPS) and the proinflammatory cytokine interferon-γ (IFNγ) to promote a classically activated M1 macrophage expressing IL-12 or conversely if exposure to IL-4 or IL-13 will promote an "alternatively activated" M2 phenotype that expresses IL-10. We predict that those studies will be completed within the next year.

Task 2: To increase the safety and controllability of the procedure through selective ablation of the cellular component of the microspheres followed by osteoclast specific resorption on the polymer, and bone healing.

We first wanted to introduce and inducible caspase 9 (icasp9$_M$) into the delivery cells so that the BMP2 production could be regulated by systemic delivery of a chemical inducer of dimerization (CID). This in turn would cause the icasp9$_M$ to become activated and initiate an apoptotic pathway leading to cell death. Therefore we generated human mesenchymal stem cells that possess a stably integrated icasp9$_M$ as well as a GFP reporter. We also obtained an MSC cell line that does not possess the icasp9$_M$ for use as an additional control. In these first experiments we determined the timing of cell death (figure 2) and determined whether this would attenuate the BMP2 expression (figure 3). We observed immediate killing of the cells greater than 95% after exposure to the CID, however, the vehicle did not lead to any significant cell death. We next looked at BMP2 expression after deliver of a single dose of CID on day 1 (figure 3). BMP2 activity was assessed through an assay in which the bone marrow cell line W20-17 will undergo osteogenic differentiation, and up regulate alkaline phosphatase activity, in the presence of active BMP2. The results suggest that the single dose of CID was able to ablate the expression of BMP2 in the cells, but the cells were capable of being efficiently transduced to produce active BMP2.

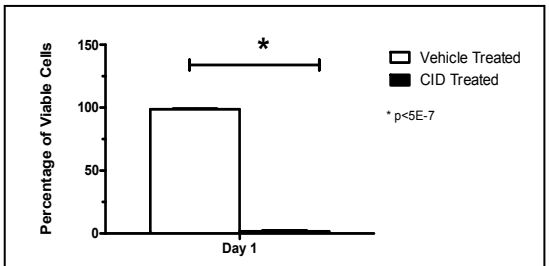

Figure 2: Cell death was immediate following delivery of the 0.1 nM chemical inducer of dimerization (CID)

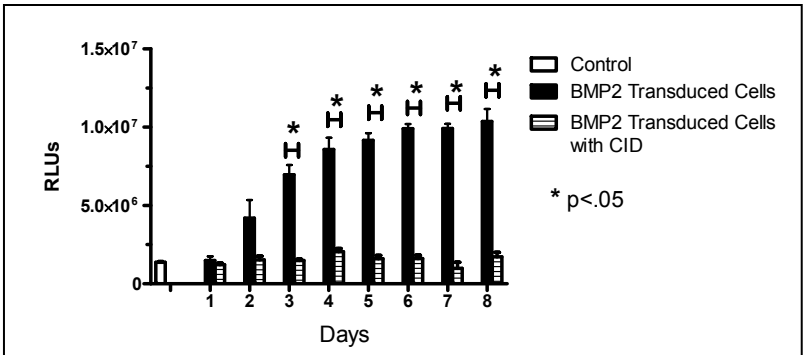

Figure 3: BMP2 activity in the presence and absence of CID. W20-17 cells were exposed for 3 days with media isolated from MSCs + icasp9$_M$ transduced with AdBMP2 (5000vp/cell) and in the presence of absence of CID. The CID was delivered on day 1, and remained in the cultures, throughout the assay.

We next attempted to encapsulate the cells and determine if they were capable of producing BMP2 to confirm that the CID would freely diffuse into the hydrogel, and activate the icasp9$_M$ similarly to the unencapsulated cells. As seen in figure 4, although the preliminary data appears to be variable, the encapsulated cells appear to produce similar amounts of the BMP2 as the unencapsulated cells. We next looked at the ability of the encapsulated cells to undergo apoptosis in the presence of CID (figure 5). These preliminary experiments suggested that within 24 hours approximately 60-75% of the cells were observed expressing the dsRED in the MSCs + icasp9$_M$, but was reduced to approximately 40% of the cells expressing the dsRED after delivery of the 0.1nM CID. Alternatively, approximately 80% were observed expressing the dsRED in the control MSCs lacking the inducible caspase 9 regardless of the presence of CID. Although preliminary these studies suggest that the CID is able to induce apoptosis in the encapsulated cells. Further studies are ongoing to follow up and optimize the kinetics and delivery of CID to the encapsulated cells.

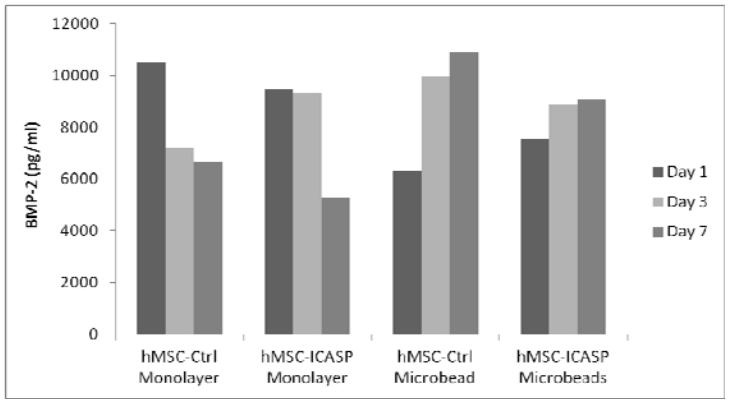

Figure 4. Comparison of BMP2 secretion in the monolayer versus the encapsulated cells.

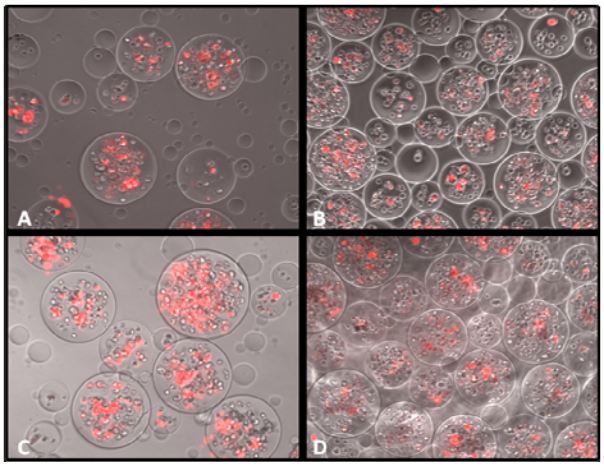

Figure 5: Comparison of dsRED expression in MSCs or MSCs + icasp9$_M$ in the presence of CID. Cells were transduced with AddsRED (5000vp/cell) and cell death was scored as the absence of red color. **(A)** hMSC-Ctrl w/o CID; **(B)** ICASP w/o CID; **(C)** hMSC-Ctrl w/ CID; **(D)** hMSC-ICASP w/ CID.

We also performed a very preliminary study to look at whether delivery of the CID could then suppress bone formation *in vivo*. In these studies, the MSCs or MSCs + icasp9$_M$ were transduced with AdBMP2 (5000vp/cell) and then injected into the rear hind-limb of NOD/Scid mice. Bone formation was detected using x-ray approximately 15 days after the initial injection (figure 6). Although there was significant variability within groups (Table 1), the trends suggest that deliver of the CID was able to suppress the bone formation when delivered earlier in the reaction (figure 6, panels A and B). However, when delivered at 11 days after initial induction of HO, the majority of the samples had significant HO (figure 6, panel C). We are currently repeating a many of these experiments to gain optimize the CID dose, and delivery time, with enough replicates to afford statistical analysis and publication. We predict that those experiments will be completed within the next year. Additionally we will initiate similar experiments in the GPSG or degradable hydrogel microspheres.

Control MSCs	**Samples with HO**
No CID	100%
CID delivered on day 1	50%
CID delivered on day 4	75%
CID delivered on day 11	50%
icasp9$_M$ MSCs	
No CID	100%
CID delivered on day 1	25%
CID delivered on day 4	25%
CID delivered on day 11	75%

Table 1: Preliminary analysis of the HO in the presence or absence of CID in MSCs and MSCs + icasp9$_M$

Task 3: To assess and compare bone quality of the skeletal and new bone during and after completion of the fusion.

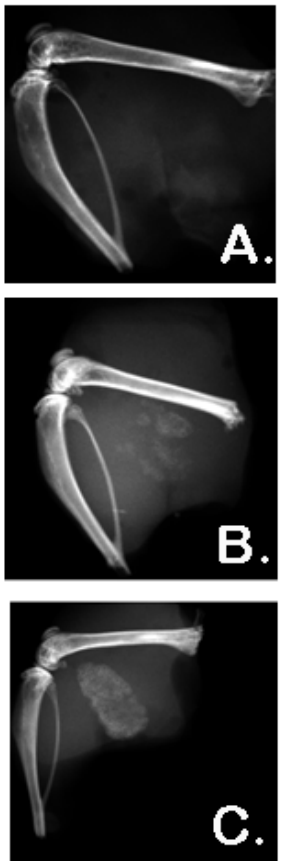

Figure 6: Radiological evaluation of bone formation 15 days after animals received AdBMP2 transduced MSCs + icasp9$_M$ followed by systemic delivery of CID **(A)** day 1, or

To accomplish this, we have developed a non-invasive optical imaging methodology to determine the optimal dose of microspheres with respect to their placement, cell viability and resultant bone formation. Therefore we altered our approach by incorporating an Alexafluor dye into the PEG hydrogel that could be detected optically. To further confirm viability of the cells, we transduced the cells with AdIFP and AdBMP2, so that we could follow the cells. Initial experiments were performed to then detect the presence of the two reporters with respect to the newly forming bone. Since this involved both optical imaging and co-alignment with microCT, we had to develop novel methodology to integrate the systems. These experiments lead to a publication of this methodology (see appendix). We propose in the next year to implement this technology using a newer reporter virus that does not interfere with the BMP2 expression, and will provide more robust bone formation. Further we will also add microPET imaging for early bone formation through detection of MMP9, which we have previously shown highlights the region where the bone matrix will be placed. From these initial findings we observed the critical nature of placement of the materials, so in this upcoming year we will focus on confirming these studies, quantifying cell viability *in vivo*, and determining optimal conditions for stabilized fusion in our rat models.

KEY RESEARCH ACCOMPLISHMENTS: We have:

- Approval of animal experiments
- Have initiated characterization of monocyte-like cells
- Have obtained stable MSC cell lines possessing the inducible caspase 9 (icasp9$_M$)
- Have demonstrated the ability of these cells to secrete BMP2 after transduction with adenovirus
- Have shown that these cells are viable after encapsulation
- Have shown that these cells respond to the CID (or activator of apoptosis) by undergoing cell death, and through the lack of BMP2 within the culture supernatant
- Have started to characterize the optimal dose of the CID to induce similar rapid cell death and suppression of the BMP2
- Have started to characterize the kinetics of in vivo delivery of CID, and resultant suppression of bone formation.
- Have developed methodology for optical detection of integrated near infrared reporters in the hydrogel microspheres
- Have developed methodology for co-localizing the optical data with microCT data of resulting bone formation.
- Published this work

REPORTABLE OUTCOMES: Provide a list of reportable outcomes that have resulted from this research to include:

- Lu Y, Darne C, Tan I, Zhu B, Hall M, Lazard Z, Davis AR, Simpson S, Sevick-Muraca EM and Olmsted-Davis EA. Far-red fluorescence gene reporter tomography for determination of placement and viability of cell-based gene therapies. Optics Express (in Press).

CONCLUSION:

We have initiated experiments to isolate and characterize the potential M2 monocyte cells that we propose are involved in rapid remodeling of the skeletal bone matrix for integration to the newly formed bone

fusion mass. In these experiments we have identified the initial cells and found that they possess several markers of the M2 lineage, which will be useful for fluorescence activated cell sorting. Once we have isolated these cells we will test their ability to resorb bone through a standard assay, and will also confirm that they behave similarly to M2 monocytes in their ability to respond to IL4 rather than proinflammatory cytokines such as LPS. These experiments are ongoing and we have not run into any problems that would prevent us from reaching our proposed goals. We have begun to establish optimal parameters for encapsulation of the MSCs + icasp9M in the PEG hydrogel microspheres that will lead to optimal bone formation. This included a number of preliminary in vitro experiments. We predict this work will be completed in the next year and we will initiate studies with the degradable form of the hydrogel. We will also continue to introduce the hydrogel microspheres through an injection into our model of spine fusion. However, due to the size and amount of microspheres, the mouse model is not practical. We have obtained fusion, but with the non-degradable form of microspheres, the fusion mass is large and often times less robust due to the large tissue area that the microspheres encompass. We have thus initiated experiments in rat models that can accommodate the large number of microspheres. In these studies, we have observed significant changes in HO as compared to the mouse. Mice readily form bone in the absence of BMP2 however, in the rat models, they do not form HO, but only orthotopic bone. We have been investigating the steps of bone formation even orthotopically in the rat models, and found that we can induce bone formation through delivery of additional cells either isolated specifically from peripheral nerves or periosteum. We are currently testing whether these cells can be bypassed by deliver of additional agents that lead to nerve remodeling (MMP9) (1)(2), which have been shown to enhance the expansion of the peripheral nerve/periosteal cells *in vivo*, and thus would potentially allow us to avoid having to deliver an additional cell type.

REFERENCES: List all references pertinent to the report using a standard journal format (i.e. format used in *Science, Military Medicine*, etc.).

1. Salisbury EA, Rodenberg E, Sonnet C, Gannon F, H. Shine D, Vadakkan T, Dickinson M, Olmsted-Davis EA, and Davis AR. Sensory Nerve Induced Inflammation Contributes to Heterotopic Ossification. J Cell Biochem. 2011 Oct;112 (10):2748-58. PMID:21678472
2. Rodenberg E, Lazard ZW, Azhdarinia A, Hall M, Kwon S, Wilganowski N, Merched-Sauvage M, Salisbury EA, Davis AR, Sevick-Muraca EM, and Olmsted-Davis EA. Matrix Metalloproteinase-9 is a Diagnostic Marker of Heterotopic Ossification in a Murine Model. Tissue Eng Part A. 2011 Oct;17(19-20):2487-96. PMID:21599541

APPENDICES:

- Lu Y, Darne C, Tan I, Zhu B, Hall M, Lazard Z, Davis AR, Simpson S, Sevick-Muraca EM and Olmsted-Davis EA. Far-red fluorescence gene reporter tomography for determination of placement and viability of cell-based gene therapies. Optics Express (in Press).

Far-red fluorescence gene reporter tomography for determination of placement and viability of cell-based gene therapies

Yujie Lu,[1,4] Chinmay D. Darne,[1] I-Chih Tan,[1] Banghe Zhu,[1] Mary A. Hall,[1] ZaWaunyka W. Lazard,[2] Alan R. Davis,[2] LaShan Simpson,[3,4] Eva M. Sevick-Muraca,[1*] and Elizabeth A. Olmsted-Davis[2]

[1]*Center for Molecular Imaging, The Brown Foundation Institute of Molecular Medicine, University of Texas Health Science Center at Houston, Houston, TX, USA*
[2]*Center for Cell and Gene Therapy, Baylor College of Medicine, Houston, Texas, USA*
[3]*Bioengineering Department, Rice University, Houston, Texas, USA*
[4]*Current address: Department of Agricultural and Biological Engineering at Mississippi State University, Mississippi State, MS, USA*
[4]*yujie.lu@uth.tmc.edu*
[*]*eva.sevick@tmc.uth.edu*

Abstract: Non-invasive injectable cellular therapeutic strategies based on sustained delivery of physiological levels of BMP-2 for spinal fusion are emerging as promising alternatives, which could provide sufficient fusion without the associated surgical risks. However, these injectable therapies are dependent on bone formation occurring only at the specific target region. In this study, we developed and deployed fluorescence gene reporter tomography (FGRT) to provide information on *in vivo* cell localization and viability. This information is sought to confirm the ideal placement of the materials with respect to the area where early bone reaction is required, ultimately providing three dimensional data about the future fusion. However, because almost all conventional fluorescence gene reporters require visible excitation wavelengths, current *in vivo* imaging of fluorescent proteins is limited by high tissue absorption and confounding autofluorescence. We previously administered fibroblasts engineered to produce BMP-2, but is difficult to determine 3-D information of placement prior to bone formation. Herein we used the far-red fluorescence gene reporter, IFP1.4 to report the position and viability of fibroblasts and developed 3-D tomography to provide placement information. A custom small animal, far-red fluorescence tomography system integrated into a commercial CT scanner was used to assess IFP1.4 fluorescence and to demark 3-D placement of encapsulated fibroblasts with respect to the vertebrae and early bone formation as assessed from CT. The results from three experiments showed that the placement of the materials within the spine could be detected. This work shows that *in vivo* fluorescence gene reporter tomography of cell-based gene therapy is feasible and could help guide cell-based therapies in preclinical models.

OCIS codes: (110.6960) Tomography; (170.3010) Image reconstruction techniques; (170.6280) Spectroscopy, fluorescence and luminescence.

References and links

1. A. S. Mistry and A. G. Mikos, "Tissue engineering strategies for bone regeneration," Adv. Biochem. Eng. Biotechnol. **94**, 1–22 (2005).
2. M. Miyazaki, H. Tsumura, J. C. Wang, and A. Alanay, "An update on bone substitutes for spinal fusion," Eur. Spine J. **18**(6), 783–799 (2009).

3. U. Heise, J. F. Osborn, and F. Duwe, "Hydroxyapatite ceramic as a bone substitute," Int. Orthop. **14**(3), 329–338 (1990).
4. H. S. An, K. Lynch, and J. Toth, "Prospective comparison of autograft vs. allograft for adult posterolateral lumbar spine fusion: differences among freeze-dried, frozen, and mixed grafts," J. Spinal Disord. **8**(2), 131–135 (1995).
5. M. P. Lutolf, F. E. Weber, H. G. Schmoekel, J. C. Schense, T. Kohler, R. Müller, and J. A. Hubbell, "Repair of bone defects using synthetic mimetics of collagenous extracellular matrices," Nat. Biotechnol. **21**(5), 513–518 (2003).
6. M. Bikram, C. Fouletier-Dilling, J. A. Hipp, F. Gannon, A. R. Davis, E. A. Olmsted-Davis, and J. L. West, "Endochondral bone formation from hydrogel carriers loaded with BMP2-transduced cells," Ann. Biomed. Eng. **35**(5), 796–807 (2007).
7. N. Ferrara, K. Houck, L. Jakeman, and D. W. Leung, "Molecular and biological properties of the vascular endothelial growth factor family of proteins," Endocr. Rev. **13**(1), 18–32 (1992).
8. A. Minamide, M. Yoshida, M. Kawakami, S. Yamasaki, H. Kojima, H. Hashizume, and S. D. Boden, "The use of cultured bone marrow cells in type I collagen gel and porous hydroxyapatite for posterolateral lumbar spine fusion," Spine **30**(10), 1134–1138 (2005).
9. M. R. Urist, "Bone: formation by autoinduction," Science **150**(3698), 893–899 (1965).
10. G. B. Bishop and T. A. Einhorn, "Current and future clinical applications of bone morphogenetic proteins in orthopaedic trauma surgery," Int. Orthop. **31**(6), 721–727 (2007).
11. K. S. Cahill, J. H. Chi, A. Day, and E. B. Claus, "Prevalence, complications, and hospital charges associated with use of bone-morphogenetic proteins in spinal fusion procedures," JAMA **302**(1), 58–66 (2009).
12. R. M. Olabisi, Z. W. W. Lazard, C. L. Franco, M. A. Hall, S. K. Kwon, E. M. Sevick-Muraca, J. A. Hipp, A. R. Davis, E. A. Olmsted-Davis, and J. L. West, "Hydrogel microsphere encapsulation of a cell-based gene therapy system increases cell survival of injected cells, transgene expression, and bone volume in a model of heterotopic ossification," Tissue Eng. Part A **16**(12), 3727–3736 (2010).
13. A. Vaccaro, "Bone morphogenetic protein and their complications," J. Bone Joint Surg. Br. **94**, 169 (2012).
14. R. M. Olabisi, Z. Lazard, M. H. Heggeness, K. M. Moran, J. A. Hipp, A. K. Dewan, A. R. Davis, J. L. West, and E. A. Olmsted-Davis, "An injectable method for noninvasive spine fusion," Spine J. **11**(6), 545–556 (2011).
15. R. Y. Tsien, "Constructing and exploiting the fluorescent protein paintbox (Nobel Lecture)," Angew. Chem. Int. Ed. Engl. **48**(31), 5612–5626 (2009).
16. K. E. Adams, S. Ke, S. Kwon, F. Liang, Z. Fan, Y. Lu, K. Hirschi, M. E. Mawad, M. A. Barry, and E. M. Sevick-Muraca, "Comparison of visible and near-infrared wavelength-excitable fluorescent dyes for molecular imaging of cancer," J. Biomed. Opt. **12**(2), 024017 (2007).
17. X. Shu, A. Royant, M. Z. Lin, T. A. Aguilera, V. Lev-Ram, P. A. Steinbach, and R. Y. Tsien, "Mammalian expression of infrared fluorescent proteins engineered from a bacterial phytochrome," Science **324**(5928), 804–807 (2009).
18. G. S. Filonov, K. D. Piatkevich, L. M. Ting, J. Zhang, K. Kim, and V. V. Verkhusha, "Bright and stable near-infrared fluorescent protein for in vivo imaging," Nat. Biotechnol. **29**(8), 757–761 (2011).
19. B. T. Feeley, A. H. Conduah, O. Sugiyama, L. Krenek, I. S. Y. Chen, and J. R. Lieberman, "In vivo molecular imaging of adenoviral versus lentiviral gene therapy in two bone formation models," J. Orthop. Res. **24**(8), 1709–1721 (2006).
20. Z. Gugala, E. A. Olmsted-Davis, F. H. Gannon, R. W. Lindsey, and A. R. Davis, "Osteoinduction by ex vivo adenovirus-mediated BMP2 delivery is independent of cell type," Gene Ther. **10**(16), 1289–1296 (2003).
21. C. D. Darne, Y. Lu, I. C. Tan, B. Zhu, J. C. Rasmussen, A. M. Smith, S. Yan, and E. M. Sevick-Muraca, "A compact frequency-domain photon migration system for integration into commercial hybrid small animal imaging scanners for fluorescence tomography," Phys. Med. Biol. **57**(24), 8135–8152 (2012).
22. A. D. Klose and E. W. Larsen, "Light transport in biological tissue based on the simplified spherical harmonics equations," J. Comput. Phys. **220**(1), 441–470 (2006).
23. M. Chu, K. Vishwanath, A. D. Klose, and H. Dehghani, "Light transport in biological tissue using three-dimensional frequency-domain simplified spherical harmonics equations," Phys. Med. Biol. **54**(8), 2493–2509 (2009).
24. Y. Lu, B. Zhu, H. Shen, J. C. Rasmussen, G. Wang, and E. M. Sevick-Muraca, "A parallel adaptive finite element simplified spherical harmonics approximation solver for frequency domain fluorescence molecular imaging," Phys. Med. Biol. **55**(16), 4625–4645 (2010).
25. Y. Lu, B. Zhu, C. Darne, I. C. Tan, J. C. Rasmussen, and E. M. Sevick-Muraca, "Improvement of fluorescence-enhanced optical tomography with improved optical filtering and accurate model-based reconstruction algorithms," J. Biomed. Opt. **16**(12), 126002 (2011).
26. Y. Lu, H. B. Machado, A. Douraghy, D. Stout, H. Herschman, and A. F. Chatziioannou, "Experimental bioluminescence tomography with fully parallel radiative-transfer-based reconstruction framework," Opt. Express **17**(19), 16681–16695 (2009).

1. Introduction

Spinal fusion is a conventional therapeutic method to reduce pain arising from abnormal motion of the vertebrae by joining two or more vertebrae with a bone substitute [1]. The

procedure is usually performed in the lumbar spine area but is also used to treat diseases in the cervical and thoracic spine regions [2]. Spinal fusion has been developed with the bone substitutes conventionally made of ceramics [3] and acquired from the donors (allograft) or from patients (autograft) [4], and more recently, made of materials generated by molecular biological methods [1]. The latter includes osteoinductive growth factors such as bone morphogenetic proteins (BMPs) [5, 6], bone healing enhanced growth factors, and mesenchymal stem cells harvested from bone marrow [7, 8]. Among the molecular biological methods, BMP-based therapeutic strategies have become popular because of their high fusion rate and ease of applicability [2].

BMP-2 was first used for bone grafting with demineralized bone matrices (DBMs) which are generated by removing the inorganic mineral and retaining the organic collagen matrix [9]. Optimal treatment requires stable, high local concentrations of BMP-2 [10–12]. Recent case reports suggest that high doses of BMP-2 leads to rapid unwanted events including osteolysis of the bone and is potentially carcinogenic [13]. *In vivo* gene therapy is a viable effective alternative since it provides similar efficacy through delivery of sustained BMP-2 expression at 100-1000 fold lower concentrations. However, direct injection of viral carriers to produce BMP-2 in the body can lead to virus uptake in other tissues than the targeted area leading to potential serious complications. Further, target regions often have limited to no tropism for the viruses, resulting in poor BMP-2 expression at the target site [2]. Techniques that involve *ex vivo* transduction of cells with BMP-2 viral vectors circumvent these problems and allow for efficient expression of the BMP-2 at the site specific area. However, the cell based strategy depends on stable cell placement at the site where therapeutic action is needed [12, 14]. Recently, we showed that poly(ethylene glycol) diacrylate (PEGDA) hydrogel is an effective carrier for encapsulation of BMP-2 producing cells enabling stable placement and allows for the use of allogenic cells, without launching an immune response that could otherwise limit BMP-2 local release [12]. Methods to longitudinally image the placement of PEGDA encapsulated BMP-2 producing cells are needed to predict cell viability and location of optimal ossification and fusion to show preclinical efficacy.

In vivo fluorescence molecular imaging has sufficient sensitivity to probe biological processes at the molecular and cellular levels by targeting specific proteins with specific probes or reporters. Fluorescence gene reporters have high specificity for target identification and can retain image-able signals with cell division, providing a unique opportunity to longitudinally monitor therapeutic response in one single mouse [15]. However, the high absorption and autofluorescence of tissues at the visible excitation wavelengths of these reporters limit non-invasive, *in vivo* fluorescence gene reporter imaging [16]. Recently, the emergence of far-red fluorescence gene reporters, such as IFP1.4 [17] and iRFP [18], promises significant improvement in the sensitivity of *in vivo* planar fluorescence imaging. Yet planar, 2-D imaging does not afford 3-D localization information, which is important to evaluate placement of encapsulated BMP-2 producing cells and predict therapeutic response [19]. Herein, we employ fluorescence tomography of the far-red fluorescence gene reporter, IFP1.4 to directly show that placement of cell based therapies can be monitored with far-red fluorescence gene reporter tomography (FGRT).

In the following, we first briefly review methods for producing IFP1.4 expressing fibroblasts and their encapsulation with PEGDA, and then describe the application of far-red fluorescence gene reporter tomography (FGRT) following the encapsulated/unencapsulated cell injection in the paraspinous muscle of mice. For this application, we developed a bi-modality (far-red fluorescence/CT) imaging system by integrating fluorescence imaging components into a Siemens Inveon scanner. A linear high-order simplified spherical harmonics approximation reconstruction algorithm with fully parallel acceleration was devised to reconstruct 3-D images detailing the position of the IFP1.4 gene reporter from 2-D projection data. The reconstructed fluorescence tomography shows the effectiveness of far-red FGRT for predicting the effect of placement of cell-based therapy.

2. Methods

2.1 Cell based gene therapy

Human diploid fetal lung fibroblasts (MRC-5) (ATCC, Manassas, VA) were propagated in Dulbecco's modified Eagle's medium at 37°C. Replication-defective E1-E3 deleted first-generation human type 5 adenoviruses (Ad) containing cDNAs for BMP-2, IFP1.4 in the E1 region of the virus were used to transduce the cells as previously described [20]. The viruses were confirmed to be negative for replication competent adenovirus and particle to plague forming unit (PFU) ratios were 1:10, 1:25, and 1:16 respectively. Briefly, viral transductions (5000 vp/cell) were done using Dulbecco's modified Eagle's medium containing 2% fetal bovine serum as describe [20].

5 x 10^6 transduced cells alone or cells encapsulated with poly(ethylene glycol) diacrylate (PEGDA) were used as previously described [12]. Three mice were intramuscularly injected with microencapsulated (N = 2) or unencapsulated (N = 1) transduced cells in the right paraspinous muscle of a mouse lumbar spine. *In vivo* fluorescence tomography and CT was performed 14-15 days after injection. Animal studies were performed in accordance with an Institutional Animal Care and Use Committee (IACUC)–approved protocols at Baylor College of Medicine and the University of Texas Health Science Center at Houston.

2.2 Bi-modality fluorescence imaging system

We previously made use of a Siemens Inveon CT gantry to realize multi-modality near-infrared fluorescence (NIRF)/PET/CT imaging system from time-dependent, frequency-domain measurements and also validated 3-D fluorescence tomography with a dual labeled imaging agent [21]. Briefly, the system consists of a gain modulatable NIR sensitive intensifier optically coupled to a front illuminated charge-coupled device (CCD) camera for detection and a modulatable NIR laser diode. Herein, we adapted system by removing the NIRF illumination source and emission filters and replaced them with a 690nm laser diode (Intense Inc., North Brunswick, NJ) and interference filters enabling tomography of IFP1.4. While the far-red gene reporter could be tomographically reconstructed using frequency-domain measurements made at 100MHz with the system, limited IFP1.4 signal required that we conducted measurments in the continuous wave (CW) mode by simply removing the RF signal.

2.3 Fluorescence gene reporter tomography (FGRT) algorithm

To simulate the photon propagation in tissues in small animals, the high-order simplified harmonics spherical (SP_N) is used to provide more accurate simulations compared to classic diffusion approximation (DA) [22–24]. We developed a fully parallel linear reconstruction algorithm for fluorescence gene reporter tomography [25]. Specifically, the SP_3 approximation in the CW mode is as follows [22–24]:

$$\begin{cases} -\nabla\bullet\dfrac{1}{3\mu_{a1}^{x,m}}\nabla\varphi_1^{x,m}+\mu_a^{x,m}\varphi_1^{x,m}-\left(\dfrac{2}{3}\mu_a^{x,m}\right)\varphi_2^{x,m}=\left[Q\mu_a^{sf}\phi^x\right]^m \\ -\left(\dfrac{2}{3}\mu_a^{x,m}\right)\varphi_1^{x,m}-\nabla\bullet\dfrac{1}{7\mu_{a3}^{x,m}}\nabla\varphi_2^{x,m}+\left(\dfrac{4}{9}\mu_a^{x,m}+\dfrac{5}{9}\mu_{a2}^{x,m}\right)\varphi_2^{x,m}=\left[-\dfrac{2}{3}Q\mu_a^{sf}\phi^x\right]^m \end{cases} \quad (1)$$

where $\varphi_{1,2}^{x,m}$ are the *composite moments* of the excitation and emission radiances; ϕ^x is the fluence of the excitation and is equal to $\varphi_1^x-\frac{2}{3}\varphi_2^x$; $\mu_{a,j}^{x,m}=\mu_a^{x,m}+\mu_s^{x,m}(1-\mathrm{g}^j)$, where $\mu_a^{x,m}$ and $\mu_s^{x,m}$ are the absorption and scattering coefficients of the tissue at excitation and emission

wavelengths, respectively; g is the anisotropic factor; and $i=1,2,3$; μ_a^{sf} and Q are the absorption coefficient and quantum efficiency of the fluorophore respectively; and $[\bullet]^m$ denotes the terms only for prediction of emission fluence. The mismatch of the refractive indices between the tissue and the external medium is considered using the corresponding boundary conditions

$$\begin{cases} \left(\dfrac{1+B_1}{3\mu_{a1}^{x,m}}\right)\nu\bullet\nabla\varphi_1^{x,m}-\left(\dfrac{D_1}{\mu_{a3}^{x,m}}\right)\nu\bullet\nabla\varphi_2^{x,m}=-\left(\dfrac{1}{2}+A_1\right)\varphi_1^{x,m}+\left(\dfrac{1}{8}+C_1\right)\varphi_2^{x,m} \\ \qquad\qquad +\left[\int_{\hat{s}\bullet\nu<0}S(\hat{s})2\left|\hat{s}\bullet\nu\right|\mathrm{d}\hat{s}\right]^x \\ -\left(\dfrac{D_2}{\mu_{a1}^{x,m}}\right)\nu\bullet\nabla\varphi_1^{x,m}+\left(\dfrac{1+B_2}{7\mu_{a3}^{x,m}}\right)\nu\bullet\nabla\varphi_2^{x,m}=\left(\dfrac{1}{8}+C_2\right)\varphi_1^{x,m}-\left(\dfrac{7}{24}+A_2\right)\varphi_2^{x,m} \\ \qquad\qquad +\left[\int_{\hat{s}\bullet\nu<0}S(\hat{s})\left(5\left|\hat{s}\bullet\nu\right|^3-3\left|\hat{s}\bullet\nu\right|\right)\mathrm{d}\hat{s}\right]^x \end{cases} \tag{2}$$

where $A_1,...,D_1,...,A_2,...,D_2$ can be found in [22]; ν is the unit outer normal of the boundary; $\hat{s}$ is the incoming direction of the excitation light; S is the excitation modulation light; and $[\bullet]^x$ represents the term used for describing excitation fluence. The measurable exiting partial current $J^{+,m,b}$ for emission is given as

$$\begin{aligned} J^{+,m,b}=&\left(\frac{1}{4}+J_0\right)\left(\varphi_1^m-\frac{2}{3}\varphi_2^m\right)-\left(\frac{0.5+J_1}{3\mu_{a1}^m}\right)\nu\bullet\nabla\varphi_1^m \\ &+\frac{1}{3}\left(\frac{5}{16}+J_2\right)\varphi_2^m-\left(\frac{J_3}{7\mu_{a3}^m}\right)\nu\bullet\nabla\varphi_2^m \end{aligned} \tag{3}$$

where the coefficients $J_0,...,J_3$ are found elsewhere [22]. With the finite element methods, we obtain the solution of $\varphi_{1,2}^x$ using Eqs. (1) and (2). Using the method described in [25], for the emission equation, we have

$$\begin{bmatrix} M_{1\varphi_1^m} & M_{1\varphi_2^m} \\ M_{2\varphi_1^m} & M_{2\varphi_2^m} \end{bmatrix}\begin{bmatrix}\varphi_1^m \\ \varphi_2^m\end{bmatrix}=\begin{bmatrix} B^m & \\ & -\dfrac{2}{3}B^m\end{bmatrix}\left[\mu_a^{sf}\right] \tag{4}$$

where B^m is obtained by its components b_{pq}^m and given as

$$b_{pq}^m=\int_\Omega Q\phi^x v_p\bullet v_q\mathrm{d}\mathbf{r} \tag{5}$$

where $v_{p,q}$ are the shape functions. By inverting the matrix on the left-hand side of Eq. (4) using similar method in [26], we have

$$\begin{cases}\varphi_1^m=\left(IM_{1\varphi_1^m}-\dfrac{2}{3}IM_{1\varphi_2^m}\right)B^m\mu_a^{sf} \\ \varphi_2^m=\left(IM_{2\varphi_1^m}-\dfrac{2}{3}IM_{2\varphi_2^m}\right)B^m\mu_a^{sf}\end{cases} \tag{6}$$

After we remove the rows in matrices $\left(IM_{1\varphi_1^m}-\frac{2}{3}IM_{1\varphi_2^m}\right)B^m$ and $\left(IM_{2\varphi_1^m}-\frac{2}{3}IM_{2\varphi_2^m}\right)B^m$ corresponding to the non-boundary measurable discretized points. We can use Eq. (3) to obtain

$$J^{+,m,b}=\beta_1\varphi_1^{m,b}+\beta_2\varphi_2^{m,b}=\left(\beta_1G_1+\beta_2G_2\right)\mu_a^{sf}=G\mu_a^{sf} \tag{7}$$

where β_1 and β_2 can be obtained using Eq. (2); G_1 and G_2 are the corresponding matrices after the operation of row removing in Eq. (6); and G is the relationship matrix betetween the unkonwn μ_a^{sf} and the acquirable measurements $J^{+,m,b}$. When there are N_v different illuminations at different positions, we have

$$J_T^{+,m,b}=A\mu_a^{sf} \tag{8}$$

where

$$J_T^{+,m,b}=\begin{bmatrix}J_1^{+,m,b}\\ \cdots\\ J_{n_v}^{+,m,b}\\ \cdots\\ J_{N_v}^{+,m,b}\end{bmatrix},\qquad A=\begin{bmatrix}G_1\\ \cdots\\ G_{n_v}\\ \cdots\\ G_{N_v}\end{bmatrix} \tag{9}$$

Finally, we can use the limited memory variable metric-bound constrained quasi-Newton method (BLMVM) to solve the following least squares problem for FGRT:

$$\min_{0<\mu_a^{sf}<\mu_a^{sf,\sup}}\theta\left(\mu_a^{sf}\right):\left\|A\mu_a^{sf}-J_T^{+,m,b}\right\|^2 \tag{10}$$

where $\mu_a^{sf,\sup}$ is the upper bound of physical constraint of μ_a^{sf}. It is noteworthy that the regularization terms are not used in the algorithm.

2.4 Small animal tomography

Mice were first imaged with CT scanner in low spatial resolution mode (with voxel length of 0.1mm) to provide whole-body surface information for registration of fluorescence measurements and tomographic reconstruction. CT scanning was then performed with high spatial resolution mode in the lumbar spine region (with voxel length of 0.06mm) in order to acquire better CT images for localizing cell placement. For fluorescence imaging, planar images of fluorescent photon distribution on the animal surface following transillumination of excitation light were acquired by rotating the optical/CT gantry to 4 different angles (0°, 45°, 180°, and 315°). For each projection, we used an aspheric lens to shape the laser to form a ~1 mm diameter point on the tissue surface. Fluorescence image integration times were varied between 300 and 1600 ms to obtain total photon count rates of approximately 40,000 and five separate images at each projection were acquired to further improve the signal-to-noise ratio (SNR) without oversaturating the limited dynamic range of the 16-bit CCD. After imaging was completed, the mice were sacrificed. The tissues of lumbar spine were extracted and were further scanned by CT with high spatial resolution mode to confirm the imaging information from *in vivo* CT images.

In order to reconstruct the far-red fluorescence tomograms from the acquired fluorescent photon distribution on the animal surface, a volumetric mesh representing the truncal region (and spine) was generated from tissue surface boundaries obtained from the low resolution CT image. Image segmentation, surface mesh generation and simplification, and tetrahedral

volumetric mesh generation were performed using the commercial software Amira 5.0 (Visualization Sciences Group, Burlington, MA). The meshes had an average element diameter of 1.0mm and the number of the discretized points ranged between 13,000 and 24,000. Using linear reconstruction algorithms, the reconstruction was performed on a cluster of eight nodes (eight CPU cores of 3.0 GHz and 16 GB RAM at each node) with input parameters of the mapped fluorescent photon distribution and uniform tissue optical properties of 0.057 mm^{-1} (absorption coefficient) and 8.50 mm^{-1} (scattering coefficient).

3. Results and discussions

3.1 Far red FGRT for spinal fusion

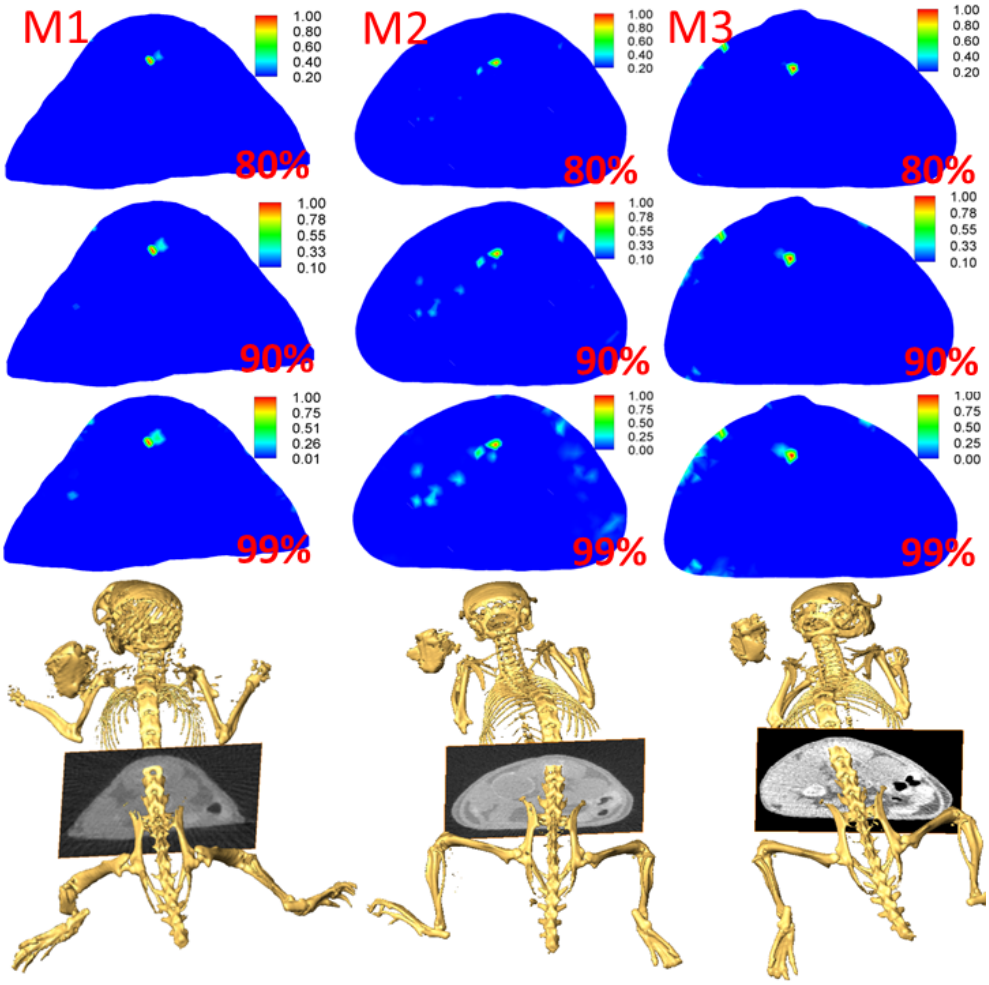

Fig. 1. The reconstructed gene reporter distribution in the cross–sections with the maximal reconstructed values (the first, second and third rows). Top 80%, 90%, and 99% reconstructed values are shown, respectively. The fourth row shows the position of the cross-sections. "M1", "M2", and "M3" are Mouse 1, 2, and 3, respectively.

Figure 1 shows the axial cross section indicating the location of the IFP1.4 gene reporter with the contour map representing the values of μ_a^{sf} thresholded to depict those values with 80%, 90%, and 99% of the maximum reconstructed values. Mouse 1 and 3 (M1 and M3) and 2 (M2) were injected with microencapsulated and unencapsulated transduced cells respectively. Due to high scattering and absorption of fluorescent photons and limited spatial resolution of

fluorescence tomography, it is generally difficult to reconstruct distributed interior objects, which may be reflected in the reconstructed results of unencapsulated cells implanted in M2. While all three reconstructed cross sections show a reconstructed fluorescent target arising from cells located at the implantation site, the axial image contains significant interior artifacts when low threshold criteria are used in the animal implanted with cells not protected by encapsulation. Although more artifacts appear in M2 compared to M1 and M3, FGRT generates one bright spot to represent the site of cell implantation. Because M1 and M3 were injected with microencapsulated cells, similar reconstruction results were obtained. Interior artifacts probably arise due to the reduced SNR associated with the loss of far-red fluorescent signals and cell viability of unencapsulated cells. Surface artifacts that occur in the reconstructions of M1 and M3 are expected and routinely filtered from the image.

3.2 Combined CT and FGRT images

Figure 2 shows new bone formation from high-resolution CT (the first column), co-registration of low resolution CT and FGRT (the second column). It is noteworthy that low resolution CT does not provide sufficient resolution for detection of early stage heterotopic bone ossification. While it is not possible to directly register high resolution CT images of heterotopic bone ossification with FGRT images derived from volumetric meshing constructed from low-resolution CT, the position of the IFP1.4 fluorescent targets co-locates in two (M1 and M2) of the three cases. In the third case with encapsulated cells, no evidence of heterotopic bone ossification was noted on high resolution CT. Due to the reduced production of BMP-2 in IFP1.4 infected fibroblasts, we could not directly correlate FGRT images with response to therapy in this initial study.

In all cases the reconstructed IFP1.4 target location corresponded to implantation site and was adjacent to vertebra in the spine. In the cases of encapsulated cell (M1, M3) and unencapsulated cell (M2) implantation in which heterotopic bone ossification occurred, mineral deposition was located between 2.2 and 2.6 mm away from the reconstructed IFP1.4 target (Table 1). (Since new bone imaging information of M3 could not be acquired from the CT images, we could not obtain quantitative compared information). The differences between fibroblast position (due to IFP1.4) and bone formation (from CT) could be explained by (i) the intrinsic localization error of fluorescence tomography, (ii) the inability to detect non-mineralized ossification tissues for accurate co-localization of BMP-2 expressing cells and heterotopic bone ossification. We have performed the imaging performance evaluation of the developed fluorescence tomography by using gold-standard nuclear imaging of dual labeled imaging agents [21] and found a smaller, but similar difference (2.15mm) between the fluorescent reconstructed results and the PET validation imaging information. The intrinsic localization error of the fluorescence tomography could contribute to the positional mismatch of fibroblast placement and eventual bone formation.

Table 1. Quantitative analysis of the CT and optical imaging information based on Fig. 2. "N.A." is due to the absence of new bone imaging information. The distance errors were calculated regarding the center positions of the new bone in the CT and optical reconstruction.

	Close to the same vertebra	*Distance from the vertebra (CT) (mm)*	*Distance between CT and Optical (mm)*
Mouse 1	Yes	0.90	2.20
Mouse 2	Yes	~0.28	2.60
Mouse 3	N.A.	N.A.	N.A.

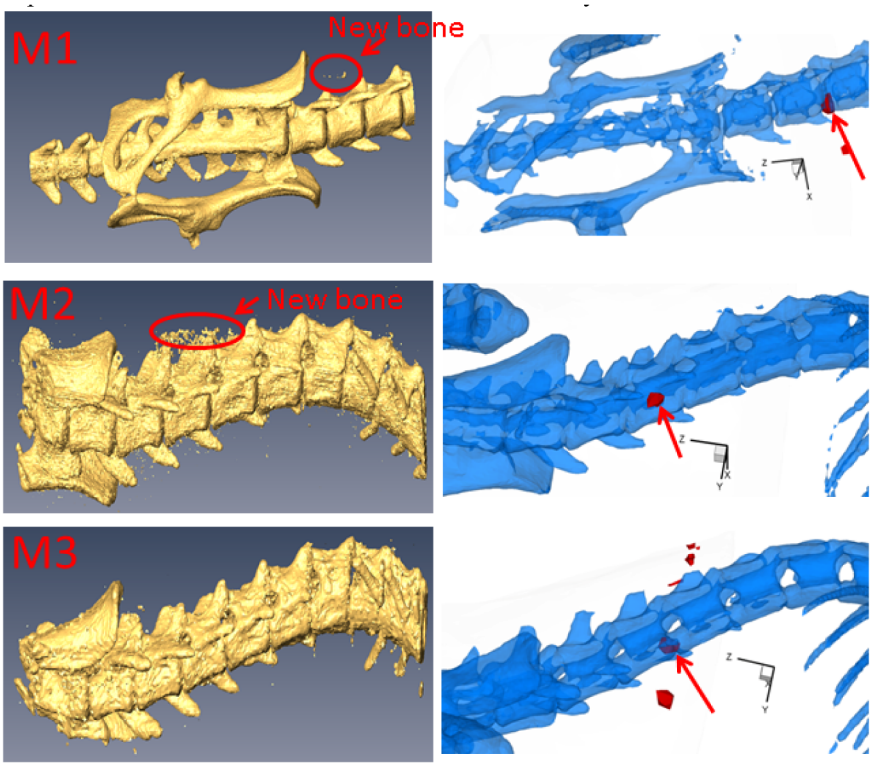

Fig. 2. The first column shows that anatomical imaging information of new bone from BMP-2 using CT scanning with high spatial resolution mode. The imaging information of new bone for M3 cannot be acquired from the CT scanning. The second column is the reconstructed results from 3-D fluorescence gene reporter tomography. The arrows show the reconstructed new bone information. “M1”, “M2”, and “M3” are Mouse 1, 2, and 3, respectively.

4. Discussions and conclusion

By avoiding the high autofluorescence background that arises from visible excitation, we have for the first time, demonstrated 3-D tomography of fluorescence gene reporters to track localization information for cell- and gene-based therapy. Due to the unexpected suppression of BMP-2 production that arises in cells expressing IFP1.4, it is difficult to observe robust functional response to therapy. However, the tomographic results from both encapsulated and unencapsulated cell-based mouse experiments show the possibility and effectiveness of fluorescence gene reporter tomography. The influence of IFP1.4 expression on the production of BMP-2 needs further investigation, whether it be towards the development of new, more innocuous fluorescence gene reporters or better methods for co-infecting fluorescent protein reporters and therapeutic proteins. In addition, although the tomographic results are promising, we assumed the tissue optical properties are homogeneous, which potentially affected the localization precision. Conventional CT scanning has low imaging contrast especially for soft tissues. We will further investigate the effect of CT contrast imaging agent in cell-based spinal fusion. The suitable one will be used to improve CT image contrast and to improve the imaging quality of fluorescence tomography. Furthermore, the lack of brightness of IFP1.4 could create anomalies associated with changing tissue absorption and scattering properties. The deployment of time-dependent FDPM measurements of image reconstruction using second generation, far-red fluorescence gene reporters with higher fluorescent yields

and less intrusive impact on expression of BMP-2 could improve the ability to correlate cell- and gene-based therapies with treatment results.

Acknowledgment

We would like to thank Dr. Jennifer L. West from the Department of Biomedical Engineering, Duke University for helping us prepare the PEGDA encapsulated BMP-2 producing cells. This work is supported by NIH R01CA135673 (EMS-M), DOD W81XWH-07-1-0215 (EO-D and ARD), W81XWH-07-1-0281(EO-D and ARD), DARPA W911NF-09-1-0040 (EO-D and ARD), and a training fellowship (YL) from the Keck Center Computational Cancer Biology Training Program of the Gulf Coast Consortia (CPRIT Grant No. RP101489).